Ocean Engineering 278 (2023) 114356

Contents lists available at ScienceDirect

Ocean Engineering

journal homepage: www.elsevier.com/locate/oceaneng

Numerical modelling of oil containment process under current and waves

Jingru Xing [a], Songgui Chen [b,*], Dimitris Stagonas [c], Liang Yang [a,*]

[a] Division of Energy and Sustainability, Cranfield University, Bedford, MK43 0AL, UK
[b] Tianjin Research Institute for Water Transport Engineering, China
[c] Department of Civil and Environmental Engineering, University of Cyprus, Cyrpus

ARTICLE INFO

Keywords:
Multi-phase level sets
One-fluid formulation
Fluid–structure interaction (FSI)
Numerical tank
Spring mooring

ABSTRACT

This study presents a novel three-phase Fluid–Structure Interaction (FSI) model for simulating the containment of oil spills. The model uses Level Sets to capture the evolution of multiple interfaces and incorporates spring forces on the structure under hybrid wave–current boundary conditions. The implementation of spring forces has been validated through simple harmonic motion models and a wedge falling simulation demonstrates the model's ability to handle multi-phase deformation. The study compares numerical results with experimental data to study the response of oil spills to wave–current hybrid conditions. Our simulations reveal that when the current exceeds 0.2 m/s, the movement of the boom is dominated by the current and not by the waves or their inertia, providing important information for the design of effective oil spill containment systems.

1. Introduction

Oil spills are a common occurrence in marine transportation, with a volume of over 15,000 tonnes reported in 2022 according to the International Tanker Owners Pollution Federation (ITOPF) (Statistics, 0000). In addition, natural seepage accounts for 45% of the yearly release of petroleum into the environment (Kvenvolden and Cooper, 2003; Board et al., 2003). These spills can cause severe pollution to freshwater and marine environments, posing a significant threat to wildlife and resources (Li et al., 2016; Jernelöv, 2010). To mitigate the spread of oil spills, the use of oil containment booms is common practice (Al-Majed et al., 2012). These booms aggregate waterborne pollutants, facilitating the isolation and disposal of contaminants. The schematic diagram for the interaction between the rigid boom and the ocean is shown in Fig. 1. The oil containment process is a multi-phase fluid–structure interaction (FSI) problem, involving the evolution of multiple fluid and solid interfaces, fluid–structure interaction with spring forces, hybrid wave–current boundary conditions, and the design of the boom, which is modelled as a rigid structure.

The system in Fig. 1 includes four phases, air Ω_a, oil Ω_o, water Ω_w and rigid boom Ω_r. The whole domain can be written as $\Omega = \Omega_a \cup \Omega_o \cup \Omega_w \cup \Omega_r$.

We present the use of the numerical wave tank (NWT) to simulate the multi-phase fluid–structure interaction problem in oil spill containment. The system in the NWT consists of multiple regions (Ω_a, Ω_o, Ω_w, and Ω_r) that are separated by their interfaces. The method of capturing these interfaces can be either mesh-based or meshless (Tryggvason et al., 2013). The Level Set Method (LSM) is a well-established mesh-based method introduced in 1988 (Sethian, 1996). In the past three decades, quite a few researchers have made more in-depth developments on LSM and it is widely used in computational geometry (Han et al., 2003), microfabrication (Sethian and Adalsteinsson, 1997), fluid dynamics (Olsson and Kreiss, 2005), image processing (Caselles et al., 1993), and computer vision (Malladi et al., 1995). Apart from LSM, the Volume of Fluid (VOF) (Hirt and Nichols, 1981; Yang et al., 2022, 2021) is another mesh-based Eulerian method for interface capturing (Yang and Stern, 2009). VOF binds the continuity, momentum and energy conservation status using volume fraction equations. This method is very convenient for the study of two-phase flow, with various applications in cloud modelling (Margolin et al., 1997), bubble motion (Tomiyama et al., 1993), fuel cells (Ferreira et al., 2015) etc. However, due to the discontinuity of the fraction function, it is difficult to achieve high-order accuracy (higher than two) of the curvature. Smoothed Particle Hydrodynamics (SPH) is a popular approach within meshless methods. The concept was originally proposed to solve interstellar hydrodynamic problems in astrophysics (Gingold and Monaghan, 1977) and has since been extended to cover many other research areas such as solid mechanics (Bonet and Kulasegaram, 2000; Cleary and Das, 2008), multi-phase flows (Shi et al., 2018), granular media flows (Peng et al., 2016), heat conduction (Chen et al., 1999), high speed impacts (Johnson et al., 1996) and underwater explosions (Liu et al., 2003), etc. However, the fluid is weakly compressible (Lind et al., 2020). For explicit accurate solutions, the time step (Δt) needs to be

* Corresponding authors.
E-mail address: liang.yang@cranfield.ac.uk (L. Yang).

https://doi.org/10.1016/j.oceaneng.2023.114356
Received 17 February 2023; Received in revised form 22 March 2023; Accepted 26 March 2023
Available online 11 April 2023

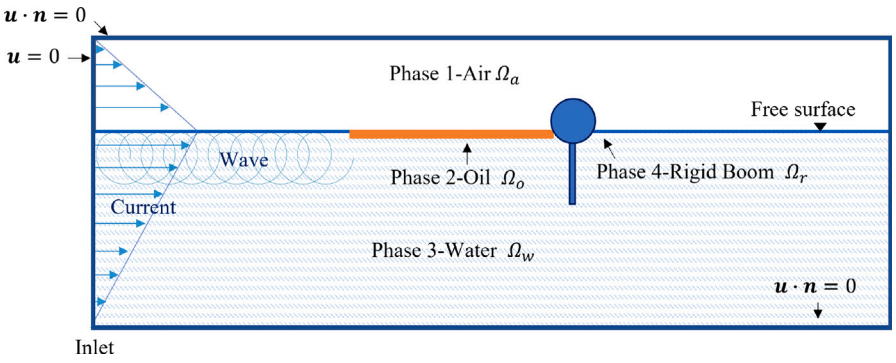

Fig. 1. Schematic diagram of the oil boom simulation.

small (Peng et al., 2019). It is also due to the nature of particles that it is relatively difficult to deal with boundary conditions, especially inlets, outlets and pressure boundary conditions, compared to mesh-based methods (Violeau and Rogers, 2016).

The simulation of fluid–structure interaction in numerical simulations can be performed using two approaches, namely the body/boundary fitted methods and the immersed type methods (Yang, 2015). The body/boundary fitted approach updates the mesh as the interface changes (Hirt et al., 1974). However, this method is computationally expensive, especially when working in 3D (Peskin, 1972). In contrast, the immersed type methods are performed on a fixed Eulerian Cartesian grid and do not require mesh updates or regeneration as the interface evolves (Peskin, 1972; Kim and Choi, 2019; Yang et al., 2016). The original concept of the Immersed Boundary Method is developed by Peskin (1972) and involves the representation of the valve's motion through a force field. The method is originally limited to solids satisfying Hooke's law (Peskin, 1977; Peskin and McQueen, 1980, 1989; McQueen and Peskin, 1989), but later, with the consideration of strain energy, it is expanded to include immersed hyperelastic solids (Peskin, 2002). Currently, the solid structure can be extended to any continuum through the introduction of the potential energy equation (Devendran and Peskin, 2012). The fluid's spatial discretisation can be built on either structured Eulerian grids or unstructured grids and adaptive local mesh refinement can be used to improve the accuracy of the method (Al-Majed et al., 2012; Roma et al., 1999). To address excessive numerical diffusion caused by the interpolation/spreading process, the Immersed Structural Potential methods were proposed (Gil et al., 2010, 2013).

The 'one-fluid' formulation is a recent addition to the family of immersed methods in fluid–structure interaction simulation (Yang, 2015; Yang et al., 2017; Yang, 2018; Yang et al., 2018a,b; Chen et al., 2021). This approach differs from traditional methods, where the dynamics of a structure are represented by a set of Newton–Euler equations, by using Lagrange multipliers to constrain the rigid motion and treating the simulated objects as fluids. The simulations are conducted on a fixed Eulerian Cartesian grid, and the Heaviside/LSM is used to capture the fluid–structure interface and eliminate indeterminate regions between the two phases. The motion of the rigid body is modelled using weighted linear least squares (Yang, 2018). The main advantage of the one-fluid approach is its computational efficiency, as it only requires a fluid solver and can handle topological changes without the need for mesh updates or re-meshing.

This paper focuses on investigating the hydrodynamic fluid–structure interaction (FSI) model using the one-fluid framework and examining its response to oil booms. The unique aspect of this study is modelling the behaviour of the mooring-boom system through a spring–mass system. The pendulum case demonstrates that the boom can rotate around a fixed point freely, while the combination of vertical and horizontal motions limited by elastic forces simulates the expected motion of a floating boom affected by waves and currents. The wedge-dropping case is designed to analyse the interaction between the rigid structure and interface deformation. The fluids in this study are treated as viscous, with clear interfaces, isothermal, and negligible surface tension effects.

The paper is organised as follows. Section 1 introduces a detailed background multi-phase FSI model. Section 2 presents a comprehensive description of the numerical method. The solutions to multi-phase interaction and computational equations are proposed. The governing equations, interface descriptions and boundary conditions are defined using the one-fluid, three-phase level set, and hybrid conditions methods. Two Simple harmonic motion (SHM) cases and the wedge-dropping model have been successfully tested using these methods. Specific descriptions and analysis are given in Section 3 and Section 4 respectively. Section 5 represents the simulation of the rigid boom in response to oil spills at sea under wave–current conditions. Finally, in Section 6, the conclusions are summarised.

2. Numerical solver

2.1. Governing equation – 'one-fluid' formulation

The dynamics of four phase system are governed by incompressible Navier–Stokes equations. Ignoring the surface tension, the conservation of the linear momentum and mass is given by Eq. (1). The different material properties are described by the deviatoric stress $\boldsymbol{f}$, see Eq. (1c).

$$\rho\left[\frac{\partial \boldsymbol{u}}{\partial t} + (\boldsymbol{\nabla u})\boldsymbol{u}\right] = -\boldsymbol{\nabla} p + \boldsymbol{f} + \rho \boldsymbol{g} \tag{1a}$$

$$\boldsymbol{\nabla} \cdot \boldsymbol{u} = 0 \tag{1b}$$

$$\boldsymbol{f} = \begin{cases} \boldsymbol{\nabla} \cdot 2\mu_a \mathbf{D}(\boldsymbol{u}) & \text{in } \Omega_a \\ \boldsymbol{\nabla} \cdot 2\mu_w \mathbf{D}(\boldsymbol{u}) & \text{in } \Omega_w \\ \boldsymbol{\nabla} \cdot 2\mu_o \mathbf{D}(\boldsymbol{u}) & \text{in } \Omega_o \\ \rho\left[\left(\frac{\partial \mathrm{P}(\boldsymbol{u})}{\partial t}\right) + (\boldsymbol{\nabla}\mathrm{P}(\boldsymbol{u}))\mathrm{P}(\boldsymbol{u})\right] + \boldsymbol{\nabla} p - \rho \boldsymbol{g} & \text{in } \Omega_r \end{cases} \tag{1c}$$

where $\mathbf{D}(\boldsymbol{u}) = \frac{1}{2}\left(\nabla \boldsymbol{u} + (\nabla \boldsymbol{u})^T\right)$ is the strain rate tensor and $\rho = \rho_a H_a + \rho_w H_w + \rho_o H_o + \rho_r H_r$ is the density. The symbols a, w, o and r stand for air, water, oil and rigid boom. $\boldsymbol{u}$ is the velocity vector field, p is the pressure, $\boldsymbol{f}$ is the force on each phase Ω, $\boldsymbol{g}$ is the gravitational acceleration, μ is the dynamic viscosity. The characteristic function χ of any region Ω_α can be uniformly expressed as

$$\chi = H_\alpha(\phi) \quad \alpha = a, w, o, r \tag{2}$$

where

$$H_\alpha(\boldsymbol{x}) = \begin{cases} 1 & \text{if } \boldsymbol{x} \in \Omega_\alpha \\ 0 & \text{if } \boldsymbol{x} \notin \Omega_\alpha \end{cases} \tag{3}$$

is a Heaviside function for any phase α (Yang, 2018). $\boldsymbol{x} = (x, y)$ is the coordinate of any point in the domain. H_α is introduced to identify different phase regions. Once the Heaviside function has been constructed, the corresponding density and viscosity field can be assigned.

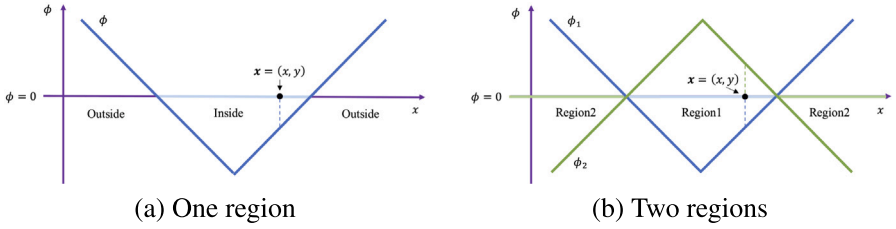

Fig. 2. Illustration of LSM in less than two regions.

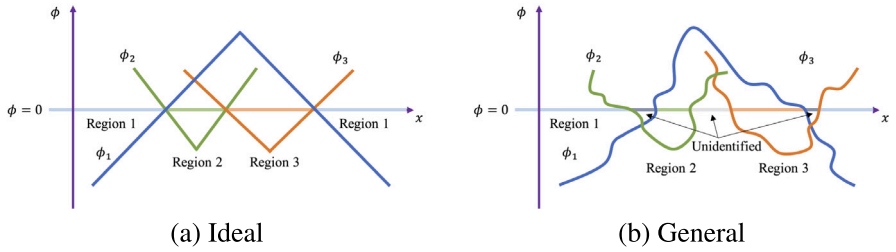

Fig. 3. Comparison of the ideal and the general situation in Multi-LSM.

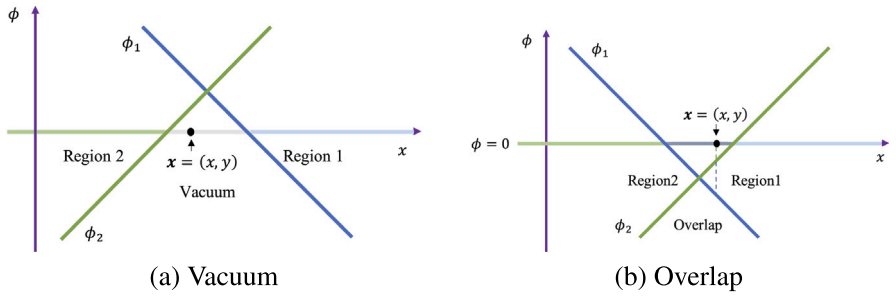

Fig. 4. Illustration of the abnormalities in Multi-LSM.

2.2. Multi-level Set Method

2.2.1. Level Set Method

LSM describes the interfaces implicitly. An object is represented by a zero contour of a level set function (LSF), which is one dimension higher than the object (Li et al., 2010). The LSF itself is a signed distance function (SDF) (Osher and Fedkiw, 2001). The evolution of the SDF formulates the motion of this object (Kass et al., 1988), see Eq. (4).

$$\phi(\boldsymbol{x}) = \operatorname{sgn} \boldsymbol{d}(\boldsymbol{x}, \Gamma) \tag{4a}$$

$$\Gamma = \left\{ \boldsymbol{x} \in \mathrm{R}^3 \mid \phi(\boldsymbol{x}, t) = 0 \right\} \tag{4b}$$

$$\phi(\boldsymbol{x}, t) \begin{cases} > 0 & \boldsymbol{x} \in \Omega_1 \\ < 0 & \boldsymbol{x} \in \Omega_2 \end{cases} \tag{4c}$$

The value of ϕ in Eq. (4a) is the shortest distance from a point $\boldsymbol{x}$ to the interface Γ. Taking a two-region system as an example (Eq. (4c)), the sign of this function represents two regions with one interface Γ, positive for region Ω_1 and negative for region Ω_2.

In non-conservative form, the evolution equation of ϕ with time can be defined by the following Eq. (5a). The LSF for three materials can be expressed as Eq. (5b).

$$\frac{\partial \phi(\boldsymbol{x}, t)}{\partial t} + \boldsymbol{u}(\boldsymbol{x}, t) \cdot \nabla \phi(\boldsymbol{x}, t) = 0 \tag{5a}$$

$$\frac{\partial \phi_\alpha(\boldsymbol{x}, t)}{\partial t} + \boldsymbol{u}(\boldsymbol{x}, t) \cdot \nabla \phi_\alpha(\boldsymbol{x}, t) = 0 \quad \alpha = 1, 2, 3 \tag{5b}$$

where $\boldsymbol{u}(\boldsymbol{x}, t)$ is the velocity of the interface. As the interface evolves, the LSF loses its signed property. To maintain this property and guarantee mass conservation, the LSF is reinitialised after each time step (Bihs et al., 2016).

2.2.2. 3-phase Level Set Method

For one-phase LSM, the expression of SDF ϕ is divided into two groups due to the location of $\boldsymbol{x}$, as shown in Fig. 2(a). ϕ is a negative number when $\boldsymbol{x}$ is inside the target region and a positive number outside. The same procedure can be adopted if two regions are within the research domain. Only need to set

$$\phi_1 = \phi \tag{6a}$$

$$\phi_2 = -\phi. \tag{6b}$$

They represent two regions in one domain, as shown in Fig. 2(b). Region 1 and region 2 correspond to those negative points in Ω_1 and Ω_2.

When extending to an arbitrary number of regions, one LSF per region is supposed to be adopted for convenience and intuitively maintain the depictions. There should be only one ϕ less than 0 (negative) in one region, while all other ϕ should be greater than 0 (positive). When the phases increase to 3 or more, and the ordinary LSM is used, the ideal distribution of regions can be demonstrated in Fig. 3(a). However, an arbitrary ϕ will introduce the vacuum and overlap (Fig. 3(b)). It is due to the generation and accumulation of numerical errors approximated by numerical solutions during the evolutionary process. More specifically, the vacuum appears when none of ϕ is negative, as shown in Fig. 4(a). No ϕ lays claim that this area belongs to any region in the domain. On the contrary, the overlap appears when more than one of ϕ is negative, as shown in Fig. 4(b). That indicates this area belongs to

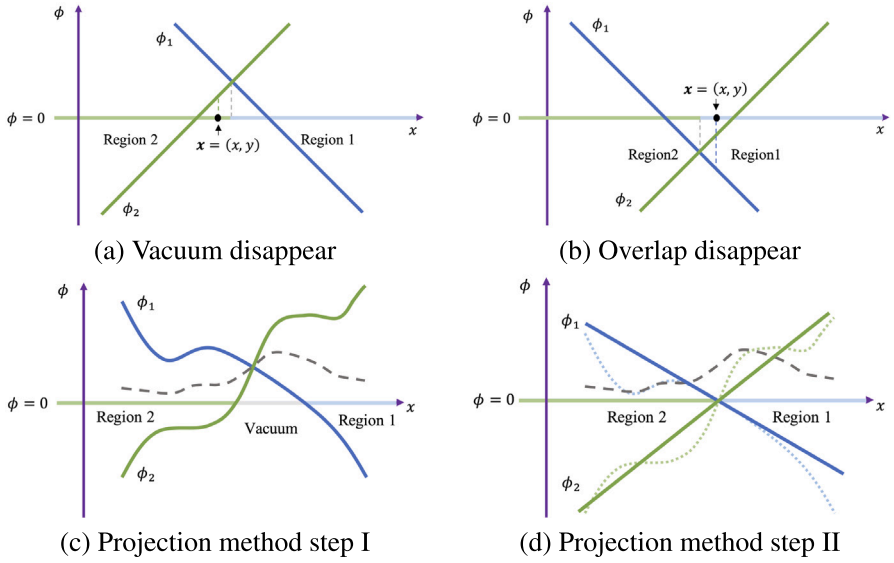

Fig. 5. Illustration of the Multi-LSM.

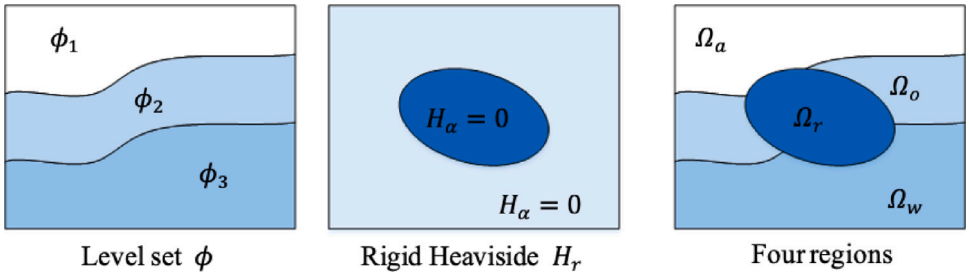

Fig. 6. The combination of the Heaviside Function and the LSM.

more than one region in the research domain. Vacuum and overlap are abnormalities during the simulation, which need to avoid.

Combining the previous experience of other researchers (Al-Majed et al., 2012; Merriman et al., 1994; Ruuth, 1998; Smith et al., 2002; Vese and Chan, 2002; Zhao et al., 1996; Losasso et al., 2006), we will use a projection scheme for the multi-LSM. To distinguish the location of the interface, each domain can be defined by the smallest level set function. For any point $\boldsymbol{x}$, if $\forall i \neq j, \phi_i < \phi_j$, then $\boldsymbol{x}$ is one point from region i. In this way, vacuum and overlap do not occur whether there are no negative ϕ or multiple negative ϕ for a given region, see Fig. 5(a) and 5(b). A projection method is proposed and applied before the standard LSM. Briefly, this projection scheme has two steps. First, find and compute the average of the two smallest level set values ϕ for every location $\boldsymbol{x}$ (Fig. 5(c)); Second, subtract this average from the original ϕ (Fig. 5(d)). Each level set can be transformed into ideal cases, like Fig. 3(a). The following Fig. 6 provides a visual representation of the combination of the multi-LSM and the Heaviside Functions applied to the oil containment process model.

In summary, we will use LSM to represent interfaces. It can automatically handle topological changes (Yang, 2015) and make it easier to calculate the normal direction and curvature of the interface. Special attention is needed for multiple Level Sets because the vacuum and overlap will appear during the simulation (Vese and Chan, 2002). Projection and initialisation procedure is added for every time step.

2.3. Numerical and discretisation scheme

The Cartesian staggered Finite Volume scheme (Marker-and-Cell grid) is adopted for the spatial discretisation of the study domain. For example, Fig. 7 shows one zoom-in part from the most refined Cartesian

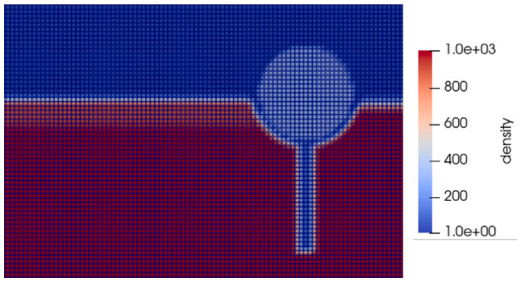

Fig. 7. Part Cartesian grid from the finest case for the rigid boom simulation (Δx = 0.0042 m).

grid for the boom simulations. The convective terms of Navier–Stokes equations are discretised with a second-order Total Variation Diminishing (TVD) Runge–Kutta scheme in the conservative framework. The fourth-order accurate Runge–Kutta scheme processes the time treatment of level set equations. Adaptive time steps are applied to govern the Courant–Friedrichs–Lewy (CFL) number. The CFL number is kept as 0.5 in this paper, which will not be repeated.

2.4. Boundary conditions

Dirichlet type, the common inlet boundary condition for free surface flow simulations, is considered the boundary condition. Dirichlet boundary condition specifies the values of related physical quantities at the boundary. For the oil containment process model, the initial wave and current profiles are based on experimental inlet settings.

Wave is generated from the point of air/water interface at the inlet, and this point is set to be the origin. Its constant motion propagates through the free surface in the positive x-axis direction, with the flow direction changing periodically. This method can generate both regular and irregular waves through the velocity equation description, but this paper only considers regular waves to maintain consistency with the experiment. In terms of the linear airy wave, the horizontal velocities u, vertical velocities v and wave profile Φ at time t can be expressed as follow (Eq. (7)) (Bihs et al., 2016).

$$u(x,z,t) = \frac{\pi H}{T}\frac{\cosh[k_w(z+d)]}{\sinh(k_w d)}\cos\theta \tag{7a}$$

$$v(x,z,t) = \frac{\pi H}{T}\frac{\sinh[k_w(z+d)]}{\sinh(k_w d)}\sin\theta \tag{7b}$$

$$\Phi(x,z,t) = \frac{H}{2}\cos\theta - z + d \tag{7c}$$

where d is the initial still water level (water depth), and z is the vertical coordinate of the wave forefront. Regarding the characteristic parameters, H is the wave height, T the wave period, $\theta = k_w x - \omega_w t$ the wave phase, $k_w = \frac{2\pi}{L}$ the wave number, L the wavelength, $\omega_w = \frac{2\pi}{T}$ the angular wave frequency. Their relationship follows the linear dispersion equation, Eq. (8).

$$L = \frac{gT^2}{2\pi}\tanh(k_w d) \tag{8}$$

The current profile (Eq. (9)) is described by a linear equation with two segments.

$$\boldsymbol{u_c} = -\frac{v_0}{s_0}s + v_0 \tag{9}$$

where $\boldsymbol{u_c}$ is the current velocity at any point; the value of $\boldsymbol{u_c}$ achieves its maximum v_0 at the air–water interface; s_0 is the thickness of the single fluid layer (air or water); s is the vertical distance from the point at the left boundary to the original air–water interface. The numerical walls of the flow domain are considered to be smooth and have the no-slip condition. The inlet of the current–wave numerical tank is the left boundary, while the right boundary is an open outlet for the flow instead of a closed wall. The sum of the regular wave and current constitutes the hybrid boundary condition. The vivid expression of the hybrid boundary conditions can be found on the left side of Fig. 1.

The ghost cell method was employed to enforce boundary conditions. A no-slip boundary condition was enforced at the bottom of the numerical wave tank by setting the horizontal and vertical velocity components (u and v) to zero in the ghost cells adjacent to the boundary.

3. The SHM simulation

3.1. Introduction

This section aims to verify the linear mooring force on the rigid structure (boom). The motion constrains include translation under spring forces and free rotation. Under the action of restoring force, the reciprocating motion of an object near its equilibrium position is called Simple Harmonic Motion (SHM). The object is subjected to the restoring force F. The force can be expressed by Eq. (10).

$$F = -kx \tag{10}$$

The force magnitude is proportional to the object displacement x, and the direction always points to the equilibrium position, where $F = 0$. For example, the simple pendulum movement, molecular microscopic motion, the movement of the object subjected to the force of the spring, et al. Such motion is characterised by periodicity. The general expressions of object $x - t$ are

$$x = A\cos(\omega t + \varphi_0) \tag{11}$$

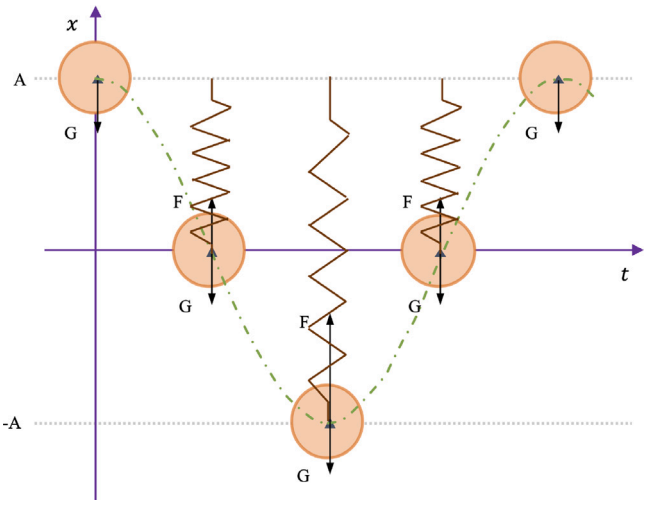

Fig. 8. A schematic representation of the variation of displacement over one cycle of the spring–mass system.

where x is the object's displacement, A is the amplitude, ω is the number of complete vibrations within 2π seconds, φ_0 is the initial phase when time $t = 0$. The vibration period of the object can be expressed by $T = \frac{2\pi}{\omega}$. The angular frequency ω of this mechanical system is

$$\omega = \sqrt{\frac{k}{m}} \tag{12}$$

which is determined by the mechanical properties of the motion system itself. m is the mass of the object.

3.2. The spring–mass oscillator

3.2.1. Spring force

A system with a spring linked to an object is called a mass spring. Within the elastic limit, the elastic force of the spring satisfies Hooke's law. According to Eq. (10), k is the spring stiffness coefficient. Fig. 8 depicts the motion of the spring–mass system over one period. In order to replicate SHM motion and build a spring–mass model, we abstract the spring by removing its entity and retaining only the characteristics of the force. That is to say, the spring itself is invisible, while the force exerted on the object will remain. The object is initially positioned at any one point in the domain. The deviation of the object x is marked with the distance from this specified point to the position at time t. The direction always points to the position calibrated at the initial moment.

The specific velocity and acceleration variations of the motion are not repeated here. When the acceleration is zero, the gravitational and restoring force on the object are balanced, and the ideal amplitude without damping can be obtained by

$$A = \frac{mg}{k} \tag{13}$$

The initial phase φ_0 is 0. g is the acceleration of gravity. The effect of the resistance is taken into account and is numerically summarised as the damping ratio ζ. Therefore, in this case, the Eq. (11) evolves into

$$x = \frac{mg}{k}e^{-\zeta t}\cos\left(\sqrt{\frac{k}{m}}t\right) \tag{14}$$

The framework considers the elastic force as the external force of the system. The connection between the spring force $\boldsymbol{F_{ext}}$ and the velocity $\boldsymbol{u_r}$ of the rigid body can be described as Eq. (15), according to the law of conservation of linear momentum.

$$\boldsymbol{F_{total}} = \boldsymbol{F_r} + \boldsymbol{F_{ext}} = m\frac{\mathrm{d}\boldsymbol{u_r}}{\mathrm{d}t} + m\frac{\mathrm{d}\boldsymbol{u_{ext}}}{\mathrm{d}t} \tag{15}$$

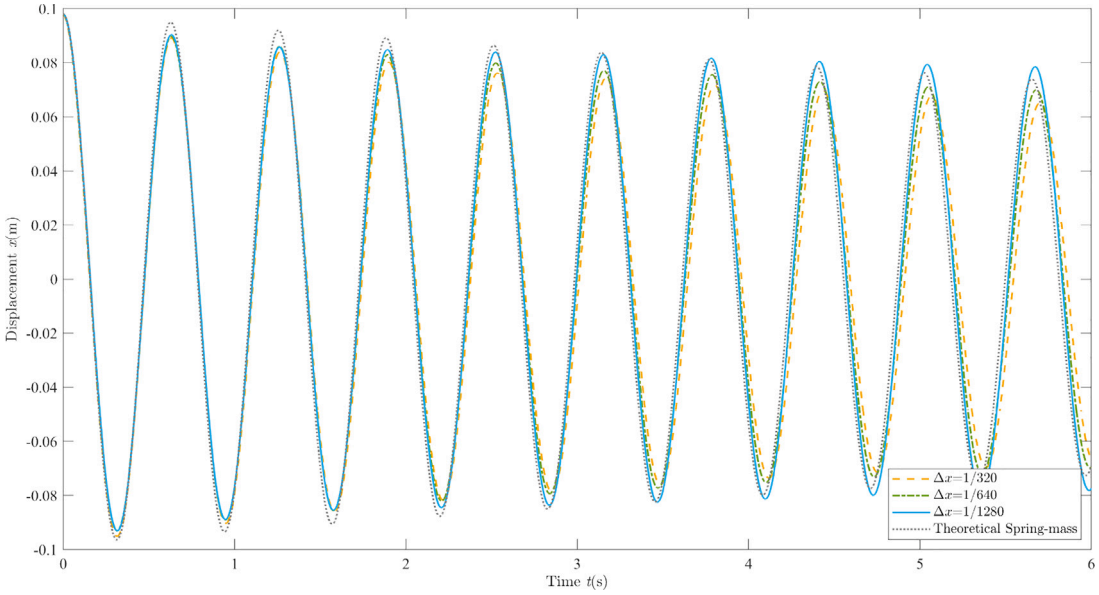

Fig. 9. Validation of convergence of spring–mass simulations and comparison with theoretical solutions (ζ=0.05).

Table 1
Grid resolution for numerical comparison of spring–mass model.

	Mesh size (m)	Numbers of cells ($x \times y$)
1	$\Delta x = \frac{1}{320} = 3.13 \times 10^{-3}$	80 × 128
2	$\Delta x = \frac{1}{640} = 1.56 \times 10^{-3}$	160 × 256
3	$\Delta x = \frac{1}{1280} = 7.81 \times 10^{-4}$	320 × 512

where $\boldsymbol{F}_{total}$ is the total force on the rigid body at each time step Δt, $\boldsymbol{u}_{ext}$ is the velocity generated by the external force (i.e. spring force in this case).

3.2.2. Numerical model setup

The target of the simulation in this section is the spring–mass system. The three-dimensional simulation system is conceptualised into a two-dimensional circle with the 'invisible' force $\boldsymbol{F}_{ext}$. The whole domain is filled with still air. Check Table 3 for its physical characteristics. In order to eliminate the effect of domain boundaries, the space around the object is deliberately left enough for its motion. This simulated object has 1 DOF, i.e. translation in the vertical direction. The main concern is the effectiveness of the simulation in applying the elastic force.

The domain size is 0.25 m×0.40 m. The object has a mass m of 1 kg and a radius r of 0.02 m. The gravitational acceleration g is 9.81 m/s^2. The spring stiffness is set to 100N/m. The value of the damping ratio ζ, in this case, is approximately 0.05, according to multiple tests. Refer to the Eq. (14), the theoretical displacement-time results of this simulation can be expressed by Eq. (16). The mass vibrates for a period of $T = \frac{2\pi}{\omega} =$ 0.63 s.

$$x = 0.098e^{-0.05t}\cos(10t) \tag{16}$$

To verify the convergence and accuracy of the numerical results, the simulation was conducted three times using structured grids of varying sizes. More details about grids can be found in Table 1.

3.2.3. Result and discussion

Fig. 9 shows the results of the numerical SHM displacement of the mass over more than ten natural periods for three grid conditions. It can be seen that the results of different grid conditions tend to converge instead of diverging at each time step, indicating that this SHM numerical model has excellent convergence. Furthermore, the numerical results are in good agreement with the theoretical results, where the data for the ascending and descending motion of the object almost coincide.

From the second period and after ($t > 0.63s$), the mass is incapable of returning to the starting position. This exemplifies the influence of the frictional damping of the surrounding air and the numerical damping of the simulation model. Besides, the frequency of the object motion does not vary significantly while the amplitude gradually decreases. In addition to the mutual conversion of kinetic and potential energy, the object constantly consumes energy to compensate for the energy dissipated by the damping. Ultimately, the object is expected to become stationary, and the spring–mass system reaches a steady state, which is a normal phenomenon in reality. If the spring-bound object is required to return to stationary more rapidly, it is only necessary to increase the spring stiffness. This phenomenon is exactly what we expect and is an essential theoretical base for why the spring system can be considered an under-damped harmonic oscillator. The spring's restoring force can be mounted on the object as a mooring force in the following CFD simulation.

3.3. The simple pendulum

3.3.1. Simple gravity pendulum

The simple gravity pendulum is an ideal physical model. A point mass (such as a ball in 3D or a circle in 2D) is connected by a massless cord and suspended from a fixed point in the gravitational field, see Fig. 10. When the mass is pulled away from the equilibrium position, i.e. the angle θ between the cord and the plumb line across the point of suspension $\neq 0$, the mass vibrates back and forth under the influence of the net restoring force $F = mg\sin\theta$. The time of one vibration is one period T. Generally speaking, when the angle θ is less than 5°, $\sin\theta \approx \frac{x}{l}$, the motion of the pendulum is linearly approximated as SHM. In this case, the restoring force is $F = -mg\frac{x}{l}$, the coefficient is $k = \frac{mg}{l}$, where m is the body mass, g is the acceleration of gravity, x is the displacement

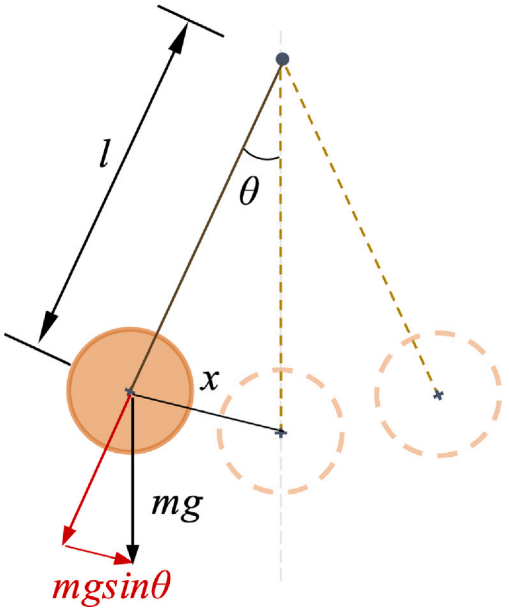

Fig. 10. Single pendulum model approximated as SHM.

and l is the cord length, as shown in Fig. 10. In summary, the motion of a single pendulum is described by the formula as Eq. (17).

$$A = \theta_0 \quad \theta|_{t=0} = \theta_0 \quad (-5° \le \theta_0 \le 5°) \tag{17a}$$

$$\theta = \theta_0 \cos\left(\sqrt{\frac{g}{l}}t + \varphi_0\right) \tag{17b}$$

$$T = \frac{2\pi}{\omega} = 2\pi\sqrt{\frac{l}{g}} \tag{17c}$$

where the amplitude A is the magnitude of the initial pendulum angle θ_0. The initial phase is $\varphi_0 = 0$. The period T is only dependent on the length l and the local acceleration of gravity g, and is irrelevant to θ_0.

Table 2
Grid resolution for numerical comparison of simple pendulum model.

	Mesh size (m)	Numbers of cells ($x \times y$)
1	$\Delta x = \frac{1}{640} = 1.56 \times 10^{-3}$	192 × 128
2	$\Delta x = \frac{1}{1280} = 7.81 \times 10^{-4}$	384 × 256
3	$\Delta x = \frac{1}{2560} = 3.91 \times 10^{-4}$	768 × 512

Table 3
Physical factors of the elements in the models.

	Density ρ_α (kg/m^3)	Kinematic viscosity ν (m^2/s)	Dynamic viscosity μ (kg/m s)
Air (20 °C)	1.204	1.516×10^{-5}	1.825×10^{-5}
Water	1000	1.000×10^{-6}	1.000×10^{-3}
Corn Oil	848	7.000×10^{-5}	5.936×10^{-2}
CKC680	890	1.625×10^{-3}	1.446

3.3.2. Numerical model setup

The single pendulum model has 1 DOF, i.e. the rotational motion. It does not translate in the horizontal or vertical direction. The massless cord is not visually labelled; only the fixed centre of rotation and its tension are retained.

The domain size is 0.30 m×0.20 m. The object has a mass m of 1 kg and a radius r of 0.01 m. The cord length l is 0.5 m. The initial pendulum angle θ_0 is −5°. The value of the damping ratio ζ, in this pendulum model, is approximately 0.14, according to multiple tests. Refer to the Eq. (17), the theoretical angle of rotation-time results for this simulation can be expressed by Eq. (18). The mass vibrates for a period of $T = 1.42$ s.

$$\theta = -5e^{-0.14t}\cos(4.43t) \tag{18}$$

The convergence is tested three times as well. The information of grids and the result is illustrated with Table 2 and Fig. 11.

3.3.3. Result and discussion

Fig. 11 demonstrates that as the grid is doubled and refined, the angle-time ($\theta - t$) curves converge more and more closely towards the

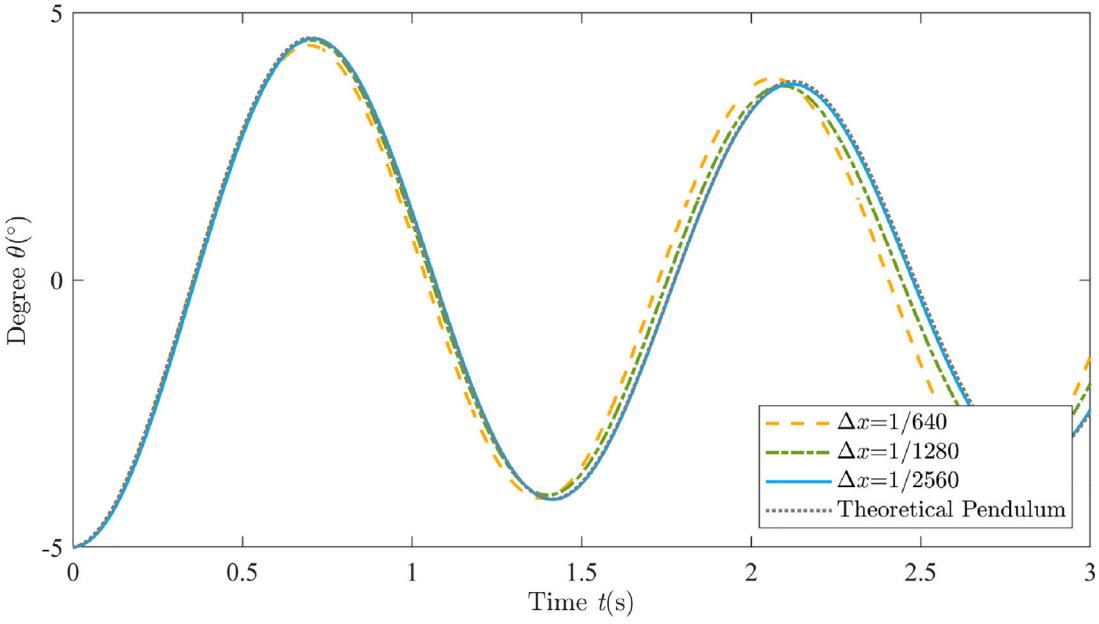

Fig. 11. Validation of convergence of pendulum simulations and comparison with theoretical solutions (ζ=0.14).

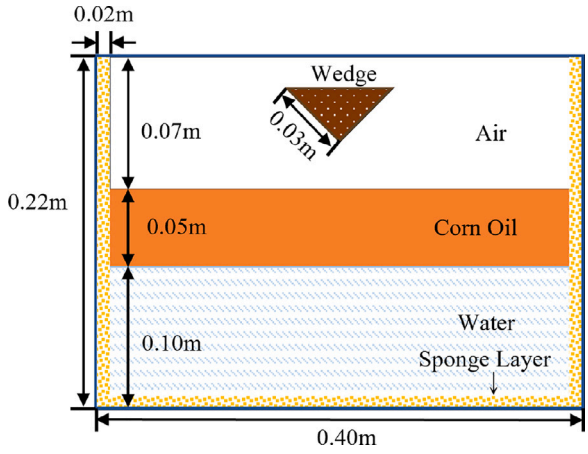

Fig. 12. A schematic diagram of the wedge dropping simulation.

theoretical values. In particular, it shows an extremely high degree of coincidence at $\Delta x = \frac{1}{2560}$ m. This proves the convergence of the present simple pendulum model. The mass is subject to the cord and gravity, oscillating near its equilibrium position around a fixed point. After one cycle of oscillation, the object returns to the position where it started to be released.

4. The dropping wedge simulation

4.1. Introduction

This chapter explores the capabilities of the one-fluid method for simulating fluid–structure interaction in multi-phase fluid environments. The wedge-dropping case is used as a test scenario to demonstrate the accuracy of the one-fluid method in modelling the interactions between rigid objects and multi-layer fluids. The wedge, as a solid body, is dropped into a calm state of a two-layer oil–water fluid, causing a disturbance and resulting in splashing. The numerical simulation will examine the effects of various physical parameters, such as the density and velocity field, on the dynamics of the fluid and the solid.

4.2. Numerical model setup

In this section, we present the numerical model setup for simulating the free-fall movement of a wedge-shaped object into a two-layer oil–water fluid system. Our model is based on the experimental setup conducted by the Tianjin Research Institute for Water Transport Engineering (TIWTE) (Shi et al., 2018). Our model is set up the same as the experiments conducted by TIWTE. Fig. 12 is a schematic diagram of the initial state position of the wedge and fluid. The entire study domain size is 0.40 m×0.22 m. The upper air part is 0.07 m thick, the middle oil layer is 0.05 m thick, and the lower water part is 0.10 m thick. The physical parameters of the oil used in the simulation are consistent with corn oil, as used in the TIWTE experiments, and are detailed in Table 3.

The wedge is modelled as a freely falling object with 3 degrees of freedom (DOF), i.e. translation in the vertical and horizontal direction, and rotational motion. The wedge has an isosceles right triangle cross-section with a right-angled side of 0.02 m and a mass of 0.2 kg. Its density is 2339.18 kg/m^3, and it starts at a distance of 0.02 m from the air–oil surface.

In order to prevent reflections from the boundaries, absorption zones with a thickness of 0.02 m are placed on the lower, left, and right sides of the domain using the relaxation method proposed by Bihs et al. (2016). The velocity components inside the absorption zone are relaxed using the equation in Eq. (19).

Table 4
Grid resolution for numerical comparison of wedge dropping model.

	Mesh size (m)	Numbers of cells ($x \times y$)
1	$\Delta x = \frac{1}{300} = 3.33 \times 10^{-3}$	120 × 66
2	$\Delta x = \frac{1}{600} = 1.67 \times 10^{-3}$	240 × 132
3	$\Delta x = \frac{1}{1200} = 8.33 \times 10^{-4}$	480 × 264

$$p(\tilde{x}) = 1 - \frac{e^{(\tilde{x}^{3.5})} - 1}{e - 1} \quad \text{for} \quad \tilde{x} \in [0, 1] \tag{19a}$$

$$u_r = p(\tilde{x}) u_o \tag{19b}$$

$$v_r = p(\tilde{x}) v_o \tag{19c}$$

where $p(\tilde{x})$ is the relaxation function and $\tilde{x}$ is a scale factor, i.e. the distance from the wave inlet boundary to the absorption zone over the entire domain length. u_r and v_r are the relaxed velocity components inside the absorption zone in the horizontal (x) and vertical (y) directions, respectively, while u_o and v_o are the original computational ones without relaxation.

The simulation was run on various grid sizes, as detailed in Table 4, and the results are analysed in Figs. 13 and 14.

In summary, the numerical model setup in this section accurately represents the experimental setup, while incorporating appropriate boundary conditions to ensure accurate and reliable results.

4.3. Result and discussion

Fig. 13 presents a series of snapshots of the wedge-dropping experiment (first row), simulation results (second row) and the corresponding velocity field (third row). The comparison charts provide a clear visual representation of the wedge's interaction with each phase at different moments. The wedge block maintains its degrees of freedom in all three directions, with no sway or rotation detected. This indicates that the horizontal direction force and the turning moment to which the wedge block is subjected are balanced. The acceleration is generated by the difference between the self-gravity and the buoyant force of the fluid. The fluid movement at the wall is effectively reduced.

The displacement D and velocity U of the simulated wedge over time are shown in Fig. 14 and demonstrate reasonable agreement with the TIWTE experiment (Shi et al., 2018). As the mesh size decreases, the differences among the results become smaller, indicating a convergent drop wedge model. The slight quantitative differences near the maximum velocity can be attributed to either the 2D simulation or numerical viscosity.

5. Oil containment process of boom simulation

5.1. Numerical model setup

5.1.1. Fluid properties

The simulation of oil spill response at sea is a representation of the interactions among air, currents, waves, oil spill and oil booms, as outlined in Section 1. The numerical model configuration replicates the experimental setup described in TIWTE (Shi et al., 2018), and the validity of the model is verified by comparing the simulation results to the experimental data. The details of the experiments and equipment can be found in the literature (Shi et al., 2018).

The overall inlet is set to the left boundary, which is the generation side of wave and current. Given that the oil boom plays a role not only in gathering the oil but also in blocking wave propagation, there is no absorption area on the right boundary. The schematic diagram of the

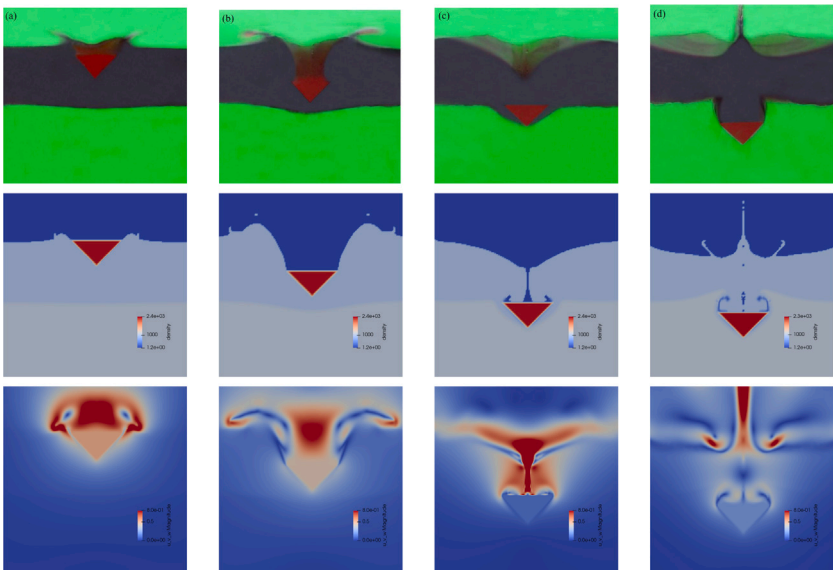

Fig. 13. Comparisons between the experiment (the 1st row) and wedge-dropping simulation ($\Delta x = \frac{1}{1200}$ m).

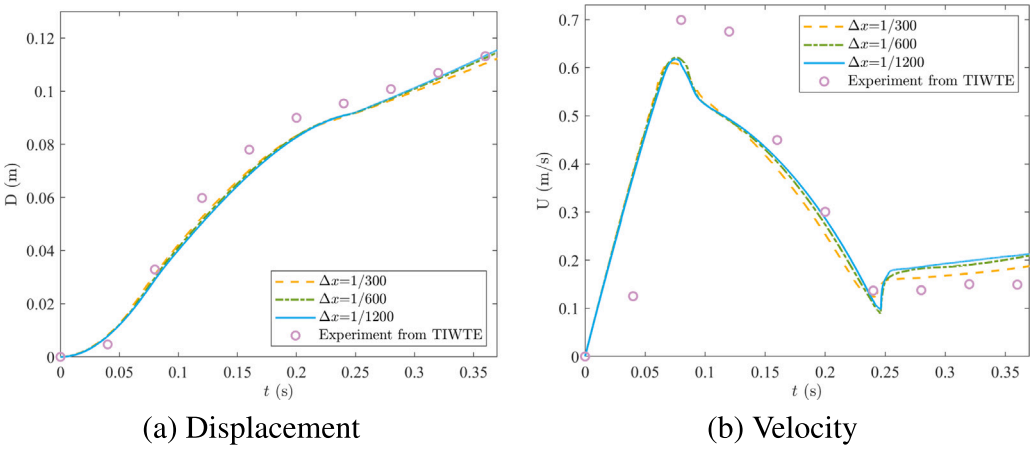

Fig. 14. The displacement and velocity of the wedge with time t.

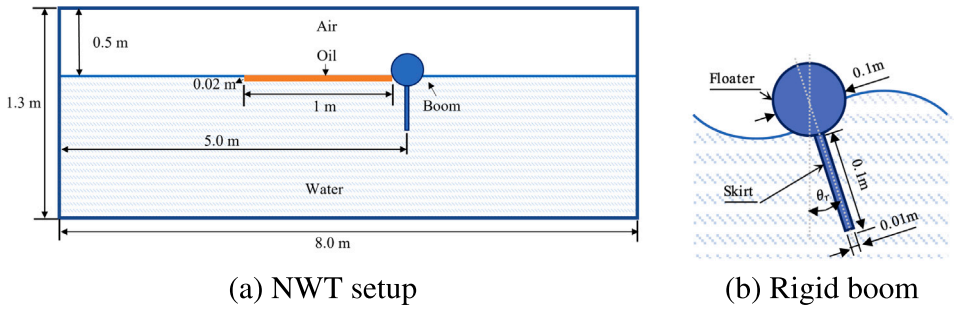

Fig. 15. A schematic diagram of the dimensions of the oil spill response simulation.

simulated initial state is shown in Fig. 15(a). The entire tank domain is 8.0 m long and 1.3 m high, with 0.5 m thick air in the upper part and 0.8 m thick water in the lower part. The oil layer is formed by the industrial gear lubricant CKC680. It floats on the surface of the water, with a length of 1 m and a thickness of 0.02 m. The boom is placed close to the right side of the oil layer, positioned 5.0 m from the left side of the tank. See Table 3 for the physical properties of the air, water and oil.

5.1.2. Rigid boom

The rigid boom model used in the simulation is a cylindrical floater with a diameter of 0.1 m and a skirt with a length of 0.1 m and a

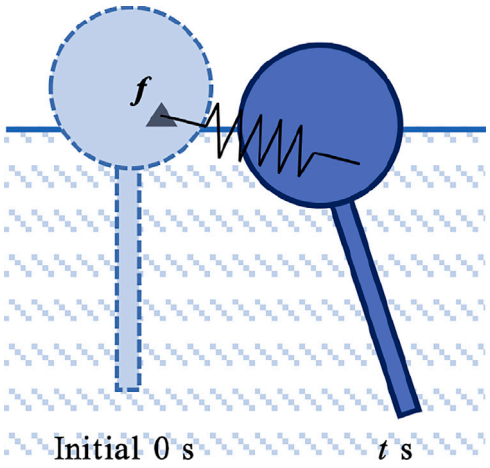

Fig. 16. The schematic representation of the mooring system.

thickness of 0.01 m, as shown in Fig. 15(b). The boom has a mass of 1.988 kg and a rotational inertia of 5.34×10^{-3} kg·m^2. The floater and skirt are treated as a single piece, and the boom's movement is represented by the whole structure's movement. The boom has 3 DOF — vertical, horizontal, and rotational motions, also described as heave, sway, and roll with rotation angle θ_r.

5.1.3. Mooring systems

Each boom is confined by an individual numerical spring force to simulate the elastic mooring system, as shown in Fig. 16. The spring attached to the boom restricts the vertical and horizontal motions, while the rotational motion is constrained by the boom's inertia, which is set to be the same as that used in the experiment. The external spring force $\boldsymbol{F}_{ext}$, represented by Eq. (20), changes as the boom deviates from its initial position and depends on the magnitude of the deviation. The deviation is measured by the change in position of a randomly selected point, marked as the anchor in the simulation, from the boom's initial position. After t seconds, the position of the anchor is the offset distance of the boom from its initial position, δx and δy.

$$\boldsymbol{F}_{ext} = \begin{bmatrix} k_1 & 0 \\ 0 & k_2 \end{bmatrix} \cdot \begin{bmatrix} \delta x \\ \delta y \end{bmatrix}, \quad \begin{cases} k_1 = 5000\ \text{kg/s}^2 \\ k_2 = 5000\ \text{kg/s}^2 \end{cases} \tag{20}$$

5.1.4. Fixed Cartesian grid

The size of the structural grid cell is 0.0042 m ($\frac{1}{240}$ m), with a total of 1926 × 318 cells (both including 6 ghost cells), see Fig. 7. The workstation is the same as above.

5.2. Result and discussion

5.2.1. Effect of current

The numerical framework was validated by comparing it to the experimental results under current conditions only. Six simulations were performed with different current speeds and the specific parameters used are listed in Table 5. The numerical simulations showed good agreement with the experimental results, as shown in Fig. 17.

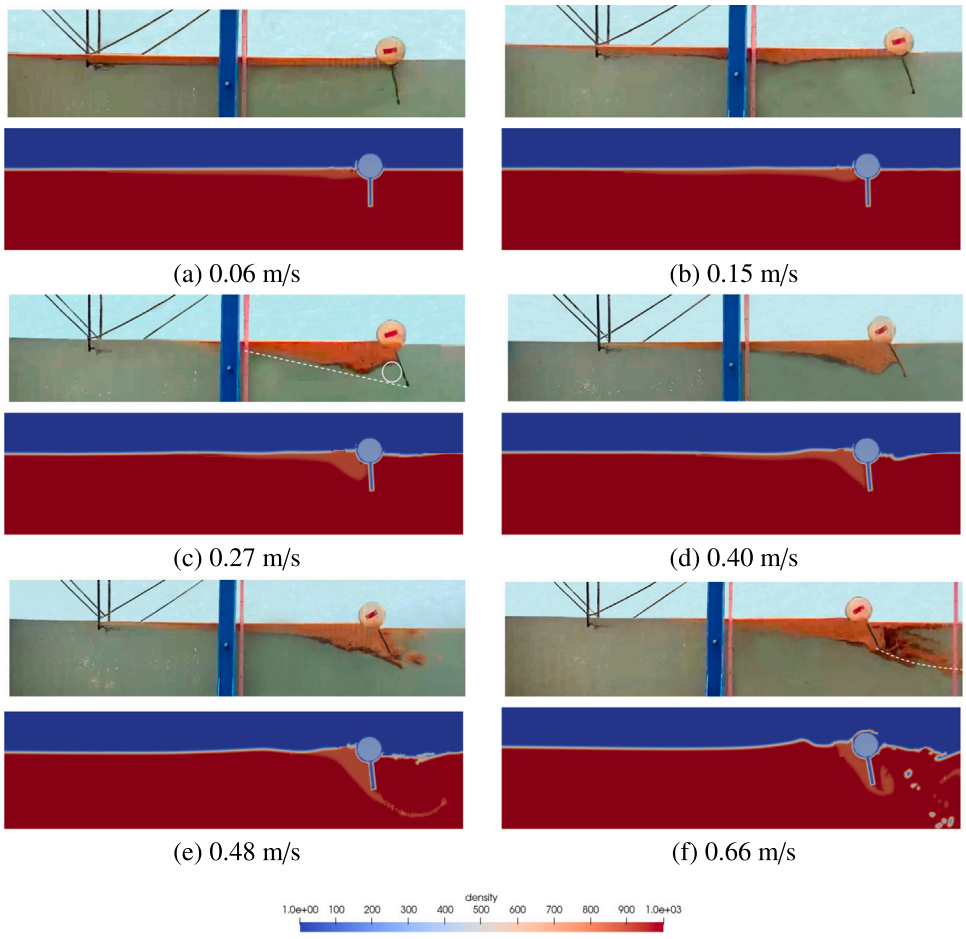

Fig. 17. The snapshots of experimental (upper) and numerical (lower) results of rigid booms at different current speed.

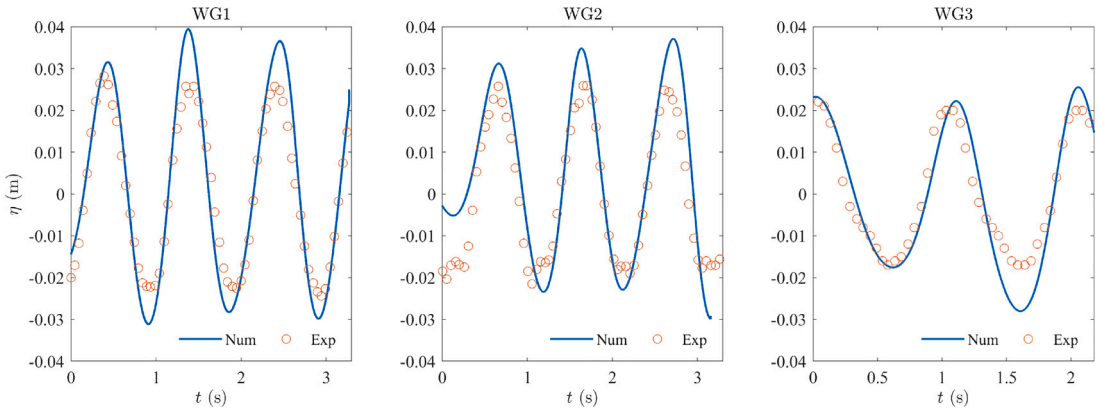

Fig. 18. Comparisons between numerical and experimental water surface elevation (U_c = 0.1 m/s).

Table 5
Current conditions in the oil spill response simulations.

Simulation	1	2	3	4	5	6
Velocity (m/s)	0.06	0.15	0.27	0.4	0.48	0.66

Table 6
Wave conditions in the oil spill response simulations.

Type	Water depth d (m)	Height H (m)	Period T (s)	Length L (m)
Airy	0.8	0.06	1.20	2.20

Table 7
Coordinates of the wave gauges while setting wave propagation as positive direction.

No. of WG	WG1	WG2	WG3
Relative position to floater initial centre (m)	−1.0	−0.5	+0.5

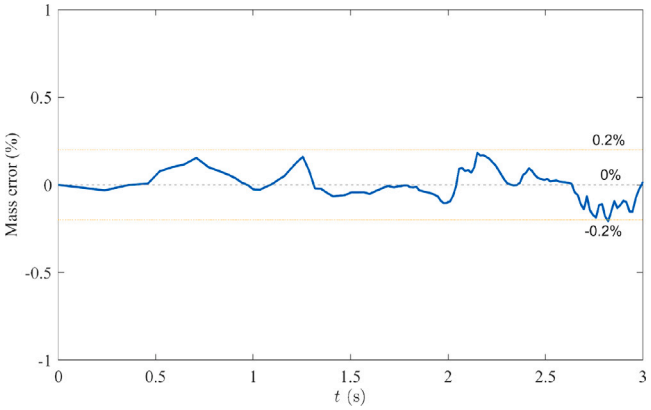

Fig. 19. The oil mass percentage error over time (Current velocity U_c = 0.1 m/s and airy wave in Table 6).

As the current velocity increased from 0.06 m/s to 0.66 m/s, the oil layer grew and accumulated towards the boom. The oscillation of the boom intensified, which helped to counteract the thrust of the thicker oil layer and prevent oil spread. No failure modes were observed in Fig. 17(a) to (d) for current speeds between 0 and 0.4 m/s. This indicates that the hybrid situation does not negatively impact the performance of the oil boom at these speeds. However, when the velocity increased to 0.48 m/s (Fig. 17(e)), small oil droplets started to escape the boom beneath the skirt and spread to the sheltered area behind it, indicating a drainage failure. At a velocity of 0.66 m/s (Fig. 17(f)), the boom moved vigorously and the oil storage capacity was weak, causing a noticeable drainage failure mode. Unlike the calm water surface in the experimental setup, the water surface in the numerical wave tank becomes more disturbed as the flow velocity increases. This is because, before the experiment, the entire system had already reached a state of equilibrium, where the boom and water surface would not have any changes under no external driving force. In the numerical wave tank, the boom is initially placed near the equilibrium state, and when the simulation starts, it tries to maintain equilibrium in the presence of the current. Due to the restoring force of the spring, the boom begins to fluctuate up and down, causing ripples in the surrounding water surface. When the flow velocity is small, the influence of the current on the equilibrium state is minimal, and the boom quickly reaches a state of equilibrium, exhibiting a great and reasonable oil containment effect. However, at high flow velocities, the interaction becomes intense, and the boom is greatly affected, even leading to Splash Over at a flow velocity of 0.66 m/s.

5.2.2. Effect of waves

This section investigates the effects of waves in a hybrid environment on the response pattern of a floating boom model. To validate the present FSI method, a quantitative validation case including waves and currents (U_c = 0.1 m/s) is presented. The parameter settings of the inlet airy wave are listed in Table 6. Three resistance-type wave gauges were used in the experiment to observe the water surface elevation, and their positions are shown in Table 7. Simulated water surface changes with the same relative position as the wave gauges and boom in the experiment were recorded and compared with the wave gauge results, see in Fig. 18. The comparison indicates a favourable agreement between the numerical simulation and experiment. Nevertheless, the amplitude of the numerical simulation slightly exceeds that of the experiment, which can be attributed to the three-dimensional effects of the experiment. Additionally, the numerical amplitude of 0.03 m is closer to the prescribed wave amplitude (i.e., a wave height of 0.06 m). These findings demonstrate the reliability and accuracy of the FSI method used in simulating oil spill response.

To account for reinitialisation at every time step, the LSF in Eq. (5) is non-conservative. However, the preservation of mass balance is still achieved and demonstrated through the calculation and presentation of the mass error percentage over time, illustrated in Fig. 19. Specifically, the mass error percentage remains within a very small range (±0.20%), indicating that the mass error is minimal and acceptable.

Next, the boom's response pattern under the influence of waves is explored for the same wave as in the validation case (Table 6) with currents up to 0.2 m/s. One wave cycle is selected to investigate the boom position under wave crest and trough, as shown in Fig. 20.

At the start of the cycle (t_1), the boom was floating upright on the water surface. Between t_1 and t_2, the boom was subject to inertia and rotated counterclockwise in a small range. At t_2, there was a slight bulge on the offshore side of the boom due to the water blockage

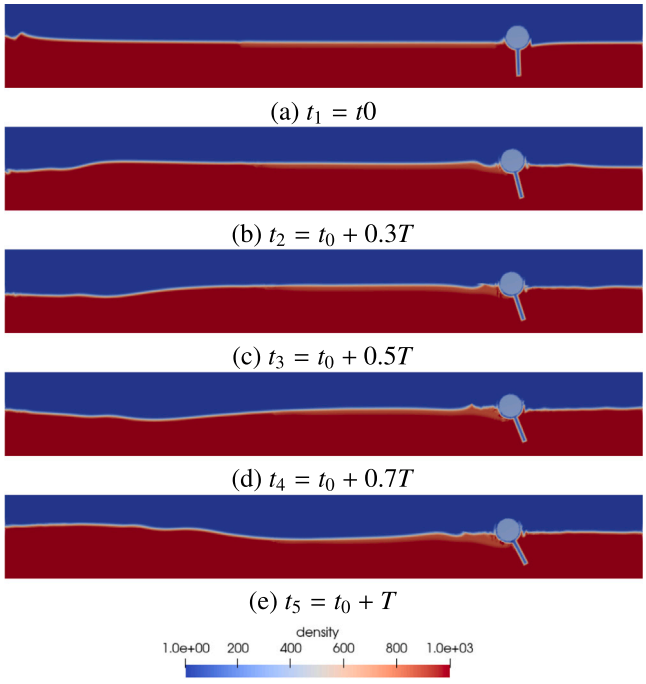

Fig. 20. The poses of a rigid boom in one wave period with 0.2 m/s current.

phenomenon. At this time, the upper part of the boom was impacted by the wave crest and the lower skirt was driven to rotate clockwise. By t_3, the boom continued to rotate counterclockwise with an increased degree of inclination, despite the periodic change in wave direction. These results suggest that at a current speed of 0.2 m/s, the motion of the boom was dominated by the current rather than the wave or its inertia. The boom continued to rotate under the wave trough until the end of the observation period (t_5) with no significant deviations, indicating that the numerical spring force effectively restrained the boom under the combined wave and current forces.

The observed response pattern of the boom under the combined influence of waves and currents is driven by several physical mechanisms, including inertia, water blockage, and wave-induced rotation. Inertia plays a role in the initial rotation of the boom, as it tends to keep the boom stationary at the moment of wave strike, effectively preventing the initial rotation. Water blockage is another factor that affects the motion of the boom. As the water hits the boom, it creates a pressure differential, which increases the hydrodynamic force acting on the boom. This increased force, combined with the inertia of the boom, helps to alleviate the severity of the rotation between t_1 and t_2. Wave-induced rotation is another mechanism that contributes to the overall motion of the boom. For the wave alone situation in Shi et al. (2018), the periodic change in wave direction leads the boom to rotate counterclockwise and then reverse, showing a periodic oscillation. However, no reverse rotation is observed in Fig. 20, suggesting that the motion of the boom was dominated by the current rather than the wave or its inertia when the current was above 0.2 m/s. By understanding these mechanisms, it is possible to design booms with features that enhance their ability to collect oil effectively in the presence of waves and currents. For instance, increasing the boom's inertia by adding weight could reduce the initial rotation caused by wave strikes, thereby improving its stability. Additionally, designing a boom with a rotational mechanism that takes advantage of wave-induced rotation could help collect oil more effectively. These design considerations could lead to more effective and reliable oil spill response strategies, ultimately reducing the environmental impact of oil spills.

6. Conclusions

The numerical framework presented in this study provides a reliable solution to the multi-phase flow problems, especially in simulating the interactions between flows and rigid structures. To maintain the conservation of mass and momentum, 'one-fluid' formulation was adopted as the governing equation. It is based on the incompressible Navier–Stokes equations and regards all the objects in the study domain as fluids. The different regions are represented by different Heaviside functions. The evolution of interfaces is captured by the 3-phase LSM to ensure the conservation of geometry. It is necessary to eliminate the vacuum and overlap and reinitialise the LSM.

Two experiments were conducted to validate the numerical model. The first experiment involved the free-fall motion of a wedge-shaped block into a two-layer water–oil fluid system. The left, bottom, and right sides of the tank were equipped with three absorption zones that simulated the effect of sponge layers. The results showed that the drop speed of the wedge rapidly increased during free fall, decreased slightly upon impact with the oil layer, and later moved at a relatively constant rate in the water layer. The second experiment was an oil spill response scenario in which a rigid boom was used to contain the spill. The boom was attached to a mooring system via a spring force. As the current speed increased from 0.06 to 0.66 m/s, the oil collected on the offshore side of the boom. Drainage failure was observed after the current speed reached 0.48 m/s. The final experiment involved the application of a hybrid wave–current boundary condition at the left inlet. The effect of the wave was studied via the performance of the rigid floating boom during a wave cycle. Further failures under this condition require further investigation.

The next step of this research will be to extend the numerical framework to three-dimensional simulations and further validate the accuracy of the results by comparing them with more experimental data. Additionally, the framework can be extended to study the impact of different parameters, such as wave height, current velocity, and oil viscosity, on the containment performance of the oil boom. These efforts will contribute to the development of effective strategies for oil spill response and environmental protection.

CRediT authorship contribution statement

Jingru Xing: Conceptualization, Software, Investigation, Visualisation, Writing – original draft. **Songgui Chen:** Supervision, Experiment, Resources. **Dimitris Stagonas:** Supervision, Writing – review & editing. **Liang Yang:** Supervision, Formal analysis, Writing – review and editing, Project administration.

Declaration of competing interest

The authors declare that they have no known competing financial interests or personal relationships that could have appeared to influence the work reported in this paper.

Data availability

No data was used for the research described in the article.

Acknowledgements

The J. Xing acknowledges the support by the China Scholarship Council (CSC) from the Ministry of Education of P.R. China. Dr L. Yang acknowledges the support by the British Council, United Kingdom, Feasibility study of hybrid propulsion for unmanned surface vehicle for environmental monitoring.

References

Al-Majed, A.A., Adebayo, A.R., Hossain, M.E., 2012. A sustainable approach to controlling oil spills. J. Environ. Manag. 113, 213–227.

Bihs, H., Kamath, A., Chella, M.A., Aggarwal, A., Arntsen, Ø.A., 2016. A new level set numerical wave tank with improved density interpolation for complex wave hydrodynamics. Comput. & Fluids 140, 191–208.

Board, O.S., Council, N.R., et al., 2003. The Oil Spill Recovery Institute: Past, Present, and Future Directions. National Academies Press.

Bonet, J., Kulasegaram, S., 2000. Correction and stabilization of smooth particle hydrodynamics methods with applications in metal forming simulations. Internat. J. Numer. Methods Engrg. 47 (6), 1189–1214.

Caselles, V., Catté, F., Coll, T., Dibos, F., 1993. A geometric model for active contours in image processing. Numer. Math. 66 (1), 1–31.

Chen, J., Beraun, J., Carney, T., 1999. A corrective smoothed particle method for boundary value problems in heat conduction. Internat. J. Numer. Methods Engrg. 46 (2), 231–252.

Chen, S., Xing, J., Yang, L., Zhang, H., Luan, Y., Chen, H., Liu, H., 2021. Numerical modelling of new flap-gate type breakwater in regular and solitary waves using one-fluid formulation. Ocean Eng. 240, 109967.

Cleary, P.W., Das, R., 2008. The potential for SPH modelling of solid deformation and fracture. In: IUTAM Symposium on Theoretical, Computational and Modelling Aspects of Inelastic Media. Springer, pp. 287–296.

Devendran, D., Peskin, C.S., 2012. An immersed boundary energy-based method for incompressible viscoelasticity. J. Comput. Phys. 231 (14), 4613–4642.

Ferreira, R.B., Falcão, D., Oliveira, V., Pinto, A., 2015. Numerical simulations of two-phase flow in proton exchange membrane fuel cells using the volume of fluid method–A review. J. Power Sources 277, 329–342.

Gil, A.J., Carreno, A.A., Bonet, J., Hassan, O., 2010. The immersed structural potential method for haemodynamic applications. J. Comput. Phys. 229 (22), 8613–8641.

Gil, A.J., Carreno, A.A., Bonet, J., Hassan, O., 2013. An enhanced immersed structural potential method for fluid–structure interaction. J. Comput. Phys. 250, 178–205.

Gingold, R.A., Monaghan, J.J., 1977. Smoothed particle hydrodynamics: theory and application to non-spherical stars. Mon. Not. R. Astron. Soc. 181 (3), 375–389.

Han, X., Xu, C., Prince, J.L., 2003. A topology preserving level set method for geometric deformable models. IEEE Trans. Pattern Anal. Mach. Intell. 25 (6), 755–768.

Hirt, C.W., Amsden, A.A., Cook, J., 1974. An arbitrary Lagrangian-Eulerian computing method for all flow speeds. J. Comput. Phys. 14 (3), 227–253.

Hirt, C.W., Nichols, B.D., 1981. Volume of fluid (VOF) method for the dynamics of free boundaries. J. Comput. Phys. 39 (1), 201–225.

Jernelöv, A., 2010. The threats from oil spills: now, then, and in the future. Ambio 39 (5), 353–366.

Johnson, G.R., Stryk, R.A., Beissel, S.R., 1996. SPH for high velocity impact computations. Comput. Methods Appl. Mech. Engrg. 139 (1–4), 347–373.

Kass, M., Witkin, A., Terzopoulos, D., 1988. Snakes: Active contour models. Int. J. Comput. Vis. 1 (4), 321–331.

Kim, W., Choi, H., 2019. Immersed boundary methods for fluid-structure interaction: A review. Int. J. Heat Fluid Flow 75, 301–309.

Kvenvolden, K., Cooper, C., 2003. Natural seepage of crude oil into the marine environment. Geo-Mar. Lett. 23 (3), 140–146.

Li, P., Cai, Q., Lin, W., Chen, B., Zhang, B., 2016. Offshore oil spill response practices and emerging challenges. Mar. Pollut. Bull. 110 (1), 6–27.

Li, C., Xu, C., Gui, C., Fox, M.D., 2010. Distance regularized level set evolution and its application to image segmentation. IEEE Trans. Image Process. 19 (12), 3243–3254.

Lind, S.J., Rogers, B.D., Stansby, P.K., 2020. Review of smoothed particle hydrodynamics: towards converged Lagrangian flow modelling. Proc. R. Soc. Lond. Ser. A Math. Phys. Eng. Sci. 476 (2241), 20190801.

Liu, M., Liu, G., Lam, K., Zong, Z., 2003. Smoothed particle hydrodynamics for numerical simulation of underwater explosion. Comput. Mech. 30 (2), 106–118.

Losasso, F., Shinar, T., Selle, A., Fedkiw, R., 2006. Multiple interacting liquids. ACM Trans. Graph. 25 (3), 812–819.

Malladi, R., Sethian, J.A., Vemuri, B.C., 1995. Shape modeling with front propagation: A level set approach. IEEE Trans. Pattern Anal. Mach. Intell. 17 (2), 158–175.

Margolin, L., Reisner, J.M., Smolarkiewicz, P.K., 1997. Application of the volume-of-fluid method to the advection–condensation problem. Mon. Weather Rev. 125 (9), 2265–2273.

McQueen, D.M., Peskin, C.S., 1989. A three-dimensional computational method for blood flow in the heart. II. Contractile fibers. J. Comput. Phys. 82 (2), 289–297.

Merriman, B., Bence, J.K., Osher, S.J., 1994. Motion of multiple junctions: A level set approach. J. Comput. Phys. 112 (2), 334–363.

Olsson, E., Kreiss, G., 2005. A conservative level set method for two phase flow. J. Comput. Phys. 210 (1), 225–246.

Osher, S., Fedkiw, R.P., 2001. Level set methods: an overview and some recent results. J. Comput. Phys. 169 (2), 463–502.

Peng, C., Bauinger, C., Szewc, K., Wu, W., Cao, H., 2019. An improved predictive-corrective incompressible smoothed particle hydrodynamics method for fluid flow modelling. J. Hydrodyn. 31 (4), 654–668.

Peng, C., Guo, X., Wu, W., Wang, Y., 2016. Unified modelling of granular media with smoothed particle hydrodynamics. Acta Geotech. 11 (6), 1231–1247.

Peskin, C.S., 1972. Flow patterns around heart valves: a numerical method. J. Comput. Phys. 10 (2), 252–271.

Peskin, C.S., 1977. Numerical analysis of blood flow in the heart. J. Comput. Phys. 25 (3), 220–252.

Peskin, C.S., 2002. The immersed boundary method. Acta Numer. 11, 479–517.

Peskin, C.S., McQueen, D.M., 1980. Modeling prosthetic heart valves for numerical analysis of blood flow in the heart. J. Comput. Phys. 37 (1), 113–132.

Peskin, C.S., McQueen, D.M., 1989. A three-dimensional computational method for blood flow in the heart I. Immersed elastic fibers in a viscous incompressible fluid. J. Comput. Phys. 81 (2), 372–405.

Roma, A.M., Peskin, C.S., Berger, M.J., 1999. An adaptive version of the immersed boundary method. J. Comput. Phys. 153 (2), 509–534.

Ruuth, S.J., 1998. A diffusion-generated approach to multiphase motion. J. Comput. Phys. 145 (1), 166–192.

Sethian, J.A., 1996. A fast marching level set method for monotonically advancing fronts. Proc. Natl. Acad. Sci. 93 (4), 1591–1595.

Sethian, J.A., Adalsteinsson, D., 1997. An overview of level set methods for etching, deposition, and lithography development. IEEE Trans. Semicond. Manuf. 10 (1), 167–184.

Shi, Y., Li, S., Chen, H., He, M., Shao, S., 2018. Improved SPH simulation of spilled oil contained by flexible floating boom under wave–current coupling condition. J. Fluids Struct. 76, 272–300.

Smith, K.A., Solis, F.J., Chopp, D., 2002. A projection method for motion of triple junctions by level sets. Interfaces Free Bound. 4 (3), 263–276.

Statistics, 0000. ITOPF. URL https://www.itopf.org/knowledge-resources/data-statistics/statistics/.

Tomiyama, A., Zun, I., Sou, A., Sakaguchi, T., 1993. Numerical analysis of bubble motion with the VOF method. Nucl. Eng. Des. 141 (1–2), 69–82.

Tryggvason, G., Dabiri, S., Aboulhasanzadeh, B., Lu, J., 2013. Multiscale considerations in direct numerical simulations of multiphase flows. Phys. Fluids 25 (3), 031302.

Vese, L.A., Chan, T.F., 2002. A multiphase level set framework for image segmentation using the Mumford and Shah model. Int. J. Comput. Vis. 50 (3), 271–293.

Violeau, D., Rogers, B.D., 2016. Smoothed particle hydrodynamics (SPH) for free-surface flows: past, present and future. J. Hydraul. Res. 54 (1), 1–26.

Yang, L., 2015. An Immersed Computational Framework for Multiphase Fluid-Structure Interaction. Swansea University (United Kingdom).

Yang, L., 2018. One-fluid formulation for fluid–structure interaction with free surface. Comput. Methods Appl. Mech. Engrg. 332, 102–135.

Yang, L., Buchan, A., Pavlidis, D., Jones, A., Smith, P., Sakai, M., Pain, C., 2021. A three-phase interpenetrating continua approach for wave and porous structure interaction. Eng. Comput. 38 (3), 1157–1169.

Yang, L., Gil, A.J., Carreño, A.A., Bonet, J., 2018a. Unified one-fluid formulation for incompressible flexible solids and multiphase flows: application to hydrodynamics using the immersed structural potential method (ISPM). Internat. J. Numer. Methods Fluids 86 (1), 78–106.

Yang, L., Lyu, Z., Yang, P., Pavlidis, D., Fang, F., Xiang, J., Latham, J.-P., Pain, C., 2018b. Numerical simulation of attenuator wave energy converter using one-fluid formulation. In: The 28th International Ocean and Polar Engineering Conference. OnePetro.

Yang, J., Stern, F., 2009. Sharp interface immersed-boundary/level-set method for wave–body interactions. J. Comput. Phys. 228 (17), 6590–6616.

Yang, J., Xu, Y., Yang, L., 2022. Taichi-LBM3D: A single-phase and multiphase lattice Boltzmann solver on cross-platform multicore CPU/GPUs. Fluids 7 (8), 270.

Yang, L., Yang, H., Yan, S., Ma, Q., 2017. Numerical investigation of water-entry problems using IBM method. Int. J. Offshore Polar Eng. 27 (02), 152–159.

Yang, L., Yang, H., Yan, S., Ma, Q., Bihnam, M., 2016. Comparative study on water impact problem. In: The 26th International Ocean and Polar Engineering Conference. OnePetro.

Zhao, H.-K., Chan, T., Merriman, B., Osher, S., 1996. A variational level set approach to multiphase motion. J. Comput. Phys. 127 (1), 179–195.